Postvoiding FEM Analysis for Electromigration Failure Characterization

Hengyang Zhao and Sheldon X.-D. Tan, *Senior Member, IEEE*

***Abstract*— In this paper, we propose a novel finite-element method-based stress analysis for void growth process after the void is nucleated in the confined copper interconnects. We focus on the postvoiding analysis of void evolution, which remains challenging and less addressed in the past because void growth leads to transient structural changes in the copper interconnects. The new method explicitly considers the stress distribution's impacts on the void volumes due to atomic conservation in confined wires. We introduce a phase-field equation that results in two coupled dynamic systems to describe the whole postvoiding stress evolution process. A novel regulated void growth velocity is introduced in order to consider the inherent physical interaction between the void volume and stress distribution in a confined interconnect wire. Numerical results show that the computed stress distributions and extracted current exponent values fit the measured results better than a recent postvoiding analysis work. Furthermore, the proposed electromigration analysis method models the Joule heating effect on wire resistance and temperature change, which were well observed in the published experiments.**

***Index Terms*— Electromigration (EM), finite-element method (FEM), IC reliability, phase-field method.**

I. Introduction

ELECTROMIGRATION (EM) is the top reliability concern for copper-based back-end-of-line interconnects of current and future ICs in 10-nm technology and below. 2014 International Technology Roadmap for Semiconductors predicts that EM lifetime of interconnects in VLSI chips will be reduced by half for each generation of nodes [1] due to the increasing current density and shrinking wireline cross-section area, which determine the critical size of EM effect.

As a result, EM-induced reliability needs to be addressed at various design stages, even at the system level to ensure reliability targets are met. However, conservative design rules based on worst cases (highest possible temperature and power consumption) and simple EM models such as Black's equation can lead to significant overdesign and 2–3× enlarged guard bands [2]. Such conservative and overdesign rules, however, will hardly remain as an option in current and future technologies because a 3× guard band increase will significantly increase the buffer size and many other aspects of chips, which can lead to increased currents, and hence, increased cost and chip power consumption. As a result, more accurate physics-based EM modeling and assessment techniques are critical for the EM-aware physical design and system-level EM lifetime optimization [3].

The currently employed method of predicting time to failure (TTF) is based on the approximation and statistical methods such as Black's equation [4] and Blech's limit [5]. They are subject to growing criticism due to their over conservativeness and lack of considerations of multisegment interconnect wires [6]. To mitigate this problem, a number of new physics-based EM modeling approaches have been proposed recently [6]–[12] based on solving Korhonen's hydrostatic stress diffusion equation [13]

$$\frac{\partial \sigma}{\partial t} = \nabla \cdot \left(\frac{D_a B}{k_B T} (\Omega \nabla \sigma - eZ\rho j) \right) \quad \text{in } \Omega_L \tag{1}$$

$$\nabla \sigma = \frac{eZ\rho j_{N_i}}{\Omega} \quad \text{on } \partial\Omega_L \cap \Gamma_{N_i}, \quad i = 1, \ldots, k \tag{2}$$

$$\nabla \sigma = \frac{\sigma}{\delta} \quad \text{on } \partial\Omega_L \cap \Gamma_{\text{void}} \tag{3}$$

where σ is the hydrostatic stress, product eZ is the effective charge of the migrating atoms, ρ is the electrical resistivity, j is the current density, k_B is Boltzmann's constant, δ is the effective thickness of the copper void boundary, T is the operating temperature, and E_a is the EM activation energy. Ω_L is the domain of simulated copper interconnect and $\partial\Omega_L$ is its boundary. Γ_{N_i} is the ith flux termination boundary, where normal current density j_{N_i} are prescribed, among k termination boundaries. Γ_{void} is the void boundary, which can be a union of several discrete voids. D_a is the atomic diffusion coefficient. D_a is given by $D_a = D_0 \exp(-(E_a/k_B T))$, where D_0 is the diffusion coefficient. Copper grain size is a key factor that affects EM lifetime [14]. Effective diffusion coefficient can be much higher in copper grain boundaries than grain bodies, which leads to different D_0 over the copper interconnect. In (1), a uniform D_0, synthesized from different body and boundary diffusion coefficients, is used. Note that Korhonen's hydrostatic diffusion equations can be applied to 3-D multisegment interconnect wires with multiple flux-termination boundary nodes, allowing any number of evolving voids to be simulated.

Equations (1)–(3) can be solved by using finite-element method (FEM) or finite-difference method in 3-D cases,

Manuscript received March 27, 2018; revised June 11, 2018; accepted July 12, 2018. Date of publication August 16, 2018; date of current version October 23, 2018. This work was supported in part by the National Science Foundation (NSF) under Grant CCF-1527324 and Grant CCF-1741961, in part by the Defense Advanced Research Projects Agency (DARPA) under Grant HR0011-16-2-0009, and in part by the University of California Institute for Mexico and the United States (UC MEXUS) under Grant CN 16-161. *(Corresponding author: Sheldon X.-D. Tan.)*

The authors are with the Department of Electrical and Computer Engineering, University of California at Riverside, Riverside, CA 92521 USA (e-mail: stan@ee.ucr.edu).

Color versions of one or more of the figures in this paper are available online at http://ieeexplore.ieee.org.

Digital Object Identifier 10.1109/TVLSI.2018.2861358

as well as 1-D or 2-D with a certain level of abstraction. In the void nucleation phase, under high current density, copper atoms are forced to slowly migrate along the electron wind direction toward the anode. Wire boundaries or terminals block such as atom migration and, consequently, tensile stress will start to be built up at the cathode, and compressive stress will develop at the anode. When the stress at the cathode reaches the critical stress, voids will form and start to grow and sometimes merge or migrate. We remark that when the compressive stress at the anode continues to be built up, hillocks or extrusion will form, which can potentially cause short-circuit failures. But the void nucleation is still the dominant EM failure effects [15].

However, it is a notoriously difficult task to simulate the postvoiding phase due to several reasons. First, void shapes or their volumes and boundaries keep changing, which makes it more difficult to model this microstructural evolution process as it requires very fine-meshed elements around the boundary. This needs dedicated adaptive remeshing method in order to keep the system matrix relatively small. Second, the void volume (shapes) and the stress distributions of the remaining wire are correlated by the following atom conservation equation [16]:

$$V_S(t) = \frac{1}{B}\int_{\Omega_L} \sigma(V,t)dV \quad \forall t \tag{4}$$

where Ω_L is the volume of remaining interconnect, V_S is the void volume, and B is the effective bulk modulus. However, most of the existing postvoid simulation methods fail to consider this void volume conservation constraint.

Method in [8] simplifies the problem into 1-D case and only considers the stress distribution without considering the void volume change and its impact on the stress distribution. Bhate *et al.* [17] proposed a 2-D FEM-based void growth analysis method by considering stress and void growth using coupled diffusion equations. In their method, Cahn–Hilliard equations are coupled to model the voids with shapes changing over time. In this method, the stress condition around the void (which should be zero) is not properly modeled. Also, it is not clear whether the conservation in (4) is satisfied.

In this paper, we try to mitigate the aforementioned problems. We propose a novel FEM-based postvoiding stress simulation technique for confined copper interconnect wires. The new method can be applied for 1-D, 2-D, and 3-D stress analysis of the wire for different tradeoffs between accuracy and speed. It provides many useful insights of the EM wear out and failure process for multisegment interconnects, which can be used to guide more compact system EM modeling and assessment methods.

The new method can perform stress analysis for both the void nucleation and void growth process. But in this paper, we focus on the postvoiding process, which is difficult to simulate due to the interaction between the void shape and stress development. Different from most of the existing EM analysis methods, which only focuses on stress evolution in the wires during the void growth phase, the new method explicitly considers the interplay between void growth and evolving stress distribution in the remaining interconnect, with physics-based conservation constraint taken into account. To this line, we introduce a separate phase field to model the void boundary evolution process, which leads to two coupled partial differential equations (PDEs) (in addition to the dynamic stress field PDE) to describe the postvoiding stress evolution process. To consider the inherent physical interaction between the void volume and stress distributions in a confined interconnect wire, a novel regulated void growth velocity is introduced, which ensures that the void volume is always consistent with the stress distribution on the wire all the time. The proposed FEM-based method models all the three regions varying over time: the void, the void boundary, and the rest of the wires based on different stress governing equations and boundary conditions. Our numerical results show that the calculated stress distribution and extracted current exponent fits the published measured results better than a recently proposed postvoiding analysis method [8]. Furthermore, the Joule heating effect is also considered in a simulation of upstream-configured copper interconnect where temperature and resistance jumps happen when the void grows to the critical volume. The proposed method can predict the unique transient wire resistance change pattern for copper interconnect wires, which were well observed by the published experimental data.

II. New Void Growth Simulation Method

In this section, we present the new FEM-based void growth simulation method, which is governed by the coupled stress diffusion and phase-field equations, to model the void boundary and dynamic stress distribution evolving over time in the copper interconnects.

Specifically, to model the interaction of hydrostatic stress σ and void shape (implied by phase field ϕ), we introduce a new phase field variable ϕ, which is defined as a unit-less function of space that represents the material by its value. As time evolves: 1) hydrostatic stress derivative leads to the atomic flux that drives the void-copper boundary to move; 2) movement of a void-copper boundary relaxes the hydrostatic stress from being built up; and 3) void volume and stress distribution conservation should be maintained. These three aspects will be discussed in Sections II-A–II-C in which the PDEs are derived to reflect the mechanisms of the interaction between σ and ϕ, as well as their evolution over time.

A. Phase Field and Weight Functions

Phase field ϕ is defined as a function of space by which the underlying material is represented. Over time, its evolution is governed by

$$\frac{\partial\phi}{\partial t} = \frac{1}{\tau_\phi}\left(\frac{\delta^2}{2}\nabla^2\phi + \phi(1-\phi^2)\right) - k_R\vec{v}\cdot\nabla\phi \tag{5}$$

where δ is the thickness of the void-copper diffusive boundary, τ_ϕ is the stabilizing time constant, k_R is the regulation factor and will be discussed in Section II-D, and $\vec{v}$ is the velocity of phase-field boundary, to be described in Section II-B. In general, domain of ϕ is locked approximately to $[-1, 1]$ by the

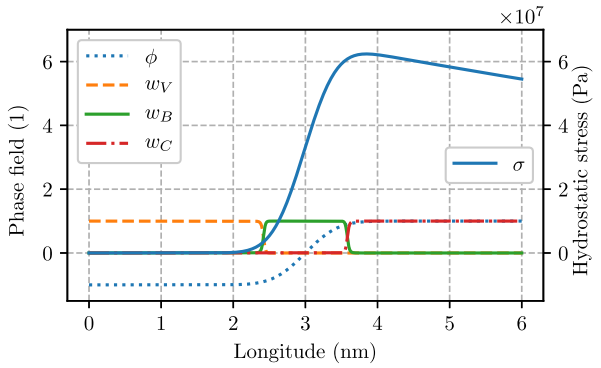

Fig. 1. Near-boundary plots of hydrostatic stress, phase field, and weight functions.

diffusion and source terms in (5). Comparing to the phase-field equation used in [8], which does not have consistent units, term τ_ϕ is introduced to control the field convergence speed, and make the units match on both sides of the equation. Materials are implied as copper if $\phi \approx 1$, void if $\phi \approx -1$, copper void boundary if $-1 < \phi < 1$. To recognize different materials in the PDEs in Sections II-A–II-C, three weight functions, w_V, w_B, and w_C, are defined as the softmax of three likelihood functions, respectively, z_V, z_B, and z_C, indicting the regions of void, boundary, and copper

$$w_V = \mathcal{S}(z_V|z_V, z_B, z_C) \tag{6}$$
$$w_B = \mathcal{S}(z_B|z_V, z_B, z_C) \tag{7}$$
$$w_C = \mathcal{S}(z_C|z_V, z_B, z_C) \tag{8}$$

where the softmax function $\mathcal{S}(z_k|z_1, z_2, \ldots, z_N)$ is defined as

$$\mathcal{S}(z_k|z_1, z_2, \ldots, z_N) = \frac{e^{z_k}}{\sum_{i=1}^{N} e^{z_i}}. \tag{9}$$

The likelihood functions depend on phase field ϕ

$$z_V = k_s \frac{-\phi - \phi_{\text{th}}}{1 - \phi_{\text{th}}} \tag{10}$$
$$z_B = k_s \frac{\phi_{\text{th}}^2 - \phi^2}{\phi_{\text{th}}^2} \tag{11}$$
$$z_C = k_s \frac{\phi - \phi_{\text{th}}}{1 - \phi_{\text{th}}} \tag{12}$$

where k_s is the sharpness coefficient and ϕ_{th} is the phase-field threshold. An illustration of σ, ϕ, w_V, w_B, and w_C near void-copper boundary is shown in Fig. 1.

B. Void-Copper Boundary Evolution

Void-copper boundary is implied by the phase-field variable ϕ. In (5), one key unknown variable is the boundary movement velocity $\vec{v}$. The relationship between $\vec{v}$ and the atomic flux J_a is

$$\vec{v} = \vec{J}_a \Omega \tag{13}$$

according to the observation of number of copper atoms moved through infinitesimal area dA

$$J_a \cdot dA \cdot dt = \frac{dV}{\Omega} = \frac{dA \cdot v dt}{\Omega}. \tag{14}$$

The flux of atoms $\vec{J}_a$ is a function of the electric field $\vec{E}$ and the gradient of chemical potential μ

$$\vec{J}_a = -\frac{D_a C_a}{k_B T}(\nabla \mu + \vec{E} q^*) \tag{15}$$

where $\mu = \mu_0 - \Omega\sigma$ and C_a denotes the copper atom concentration. On void-copper boundary where the normal vector is denoted by $\vec{n}$, we have $\vec{E} \cdot \vec{n} = 0$, which leads the following simplification:

$$\vec{J}_a \cdot \vec{n} = -\frac{D_a C_a}{k_B T}(\nabla \mu) \cdot \vec{n} = \frac{D_a C_a}{k_B T} \Omega \nabla \sigma \cdot \vec{n}. \tag{16}$$

Applying the approximation $C_a \Omega \approx 1$, we get the boundary movement velocity

$$\vec{v} \cdot \vec{n} = \frac{D_a \Omega}{k_B T} \nabla \sigma \cdot \vec{n}. \tag{17}$$

By substituting $\vec{v}$ in (5) using (17), the evolution of phase field ϕ regulated by $\nabla\sigma$ is described as

$$\frac{\partial \phi}{\partial t} = \frac{1}{\tau_\phi}\left(\frac{\delta^2}{2}\nabla^2\phi + \phi(1 - \phi^2)\right) - k_R \frac{D_a \Omega}{k_B T} \nabla \sigma \cdot \nabla \phi. \tag{18}$$

Note that $\nabla\sigma$ is the stress gradient on void-copper interface as depicted in Fig. 1.

C. Hydrostatic Stress Modeling in Confined Metal Wires

Hydrostatic stress σ in the confined metal wire has different governing equations that need to be separately derived for void, void-copper boundary, and copper.

1) Governing Equation of σ in Copper: In confined copper, hydrostatic stress σ builds up over time [13]

$$\frac{\partial \sigma}{\partial t} = \nabla \cdot \left(\frac{D_a B}{k_B T}(\Omega \nabla \sigma + eZ\rho j)\right). \tag{19}$$

2) Governing Equation of σ on Void-Copper Boundary Interface: On a void-copper boundary interface, source term $eZ\rho j$ in (19) is dropped since there is no current flowing in the normal direction. As the boundary moves with a certain speed, σ decreases as a relaxation effect of the void growth and the consequent copper atom migration. At a certain point in copper, it takes $\Delta t = (\delta/v)$ for the boundary to leave since its inclusion. During Δt, stress σ is reduced to zero from the original value when it was included in the void-copper boundary. A term $-(\sigma v k_\tau/\delta)$ is therefore added to the right-hand side to model this behavior

$$\frac{\partial \sigma}{\partial t} = \nabla \cdot \left(\frac{D_a B \Omega}{k_B T} \nabla \sigma\right) - \frac{\sigma v k_\tau}{\delta} \tag{20}$$

where k_τ is the speed-up factor which ensures that the stress is relaxed to a near-zero level.

3) Governing Equation of σ Inside a Void: Once a void has nucleated, which is typically at or near a terminal node, the stress at the void location will immediately vanish. However, the stress around the void will be close to the same stress level as immediately prior to the nucleation [8], [13]. As a result, a very large stress gradient will be formed around

the void at nucleation time, which can be described by [13]. The hydrostatic stress of copper inside a void is governed by

$$\frac{\partial \sigma}{\partial t} = \frac{\sigma}{\tau_{\text{void}}} \tag{21}$$

where τ_{void} is the vanishing time constant to ensure σ valued at 0 in the void.

4) Combined Final Governing Equation: To consider the three equations together in domain Ω_L, weight functions introduced in Section II-A are used to combine them into one PDE

$$\frac{\partial \sigma}{\partial t} = w_C \nabla \cdot \left(\frac{D_a B}{k_B T} (\Omega \nabla \sigma + eZ\rho j) \right) + w_V \frac{\sigma}{\tau_{\text{void}}} + w_B \left(\nabla \cdot \left(\frac{D_a B \Omega}{k_B T} \nabla \sigma \right) - \frac{\sigma \upsilon k_\tau}{\delta} \right). \tag{22}$$

D. Conservation Enforcement by Relating Void Volume and Hydrostatic Stress Distribution

To enforce the conservation equation (4), one approach is to introduce a closed-loop feedback between the two coupled PDE systems so that if the volumes computed by the stress distribution and the actual void volume are not equal, the void boundary growth speed will be adjusted. To achieve this, we need to compute the void volume in two different ways which are equivalent in terms of continuum physics.

Specifically, according to the definition of weight functions, the modeled void volume can be calculated by integrating an appropriate combination of w_B and w_V

$$V_W(t) = \int_{\Omega_L} \left(w_V(t) + \frac{1}{2} w_B(t) \right) dV \quad \forall t. \tag{23}$$

In addition, the stress and the void saturation volume need to satisfy the relationship defined in (4): $V_S(t) = (1/B) \int_{\Omega_L} \sigma(V, t) dV$. Due to the large atom flux at the void-copper boundary, atoms can diffuse into the whole copper interconnect rapidly if the void volume and stress distribution interaction are not considered. This will manifest the growing discrepancy between V_W and V_S over time. To mitigate this problem, we introduce a new regulation factor k_R in phase-field governing equation (5) and (18)

$$k_R(t) = \frac{1}{2}(1 + \text{erf}(V_W(t) - V_S(t))) \tag{24}$$

where $\text{erf}(\cdot)$ is the Gauss error function to force a bounded output range $(-1, 1)$. As a result, the regulated velocity of the void shape boundary will be expressed as $\vec{v} k_R(t)$. Consequently, if the $V_W(t)$ is larger than V_S, $k_B(t)\vec{v}$ will increase so that the void volume, V_S, will increase as well, which will make the difference between the two volumes smaller. This is also the case when $V_W(t)$ is smaller than V_S. Fig. 2 shows the modeled void volume V_W being consistent with the void saturation volume V_S from the proposed simulation method.

III. Finite-Element Method Implementation

In this section, variational formulations that are implemented in the simulation software are listed, followed by the description of adaptive local mesh refinement and a brief review of the software architecture.

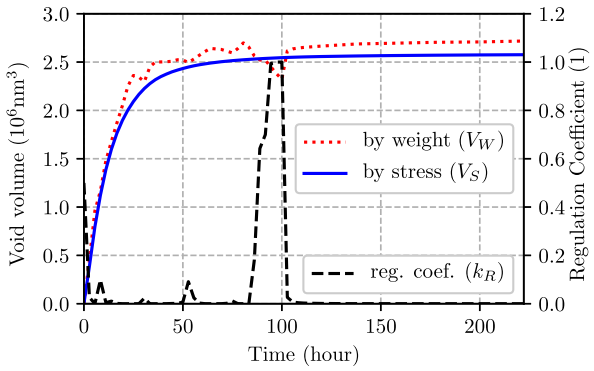

Fig. 2. Void volume calculated by weight functions (V_W) and by stress (V_S) over time.

A. Variational Formulation

Based on deal.II FEM library [18], a program is built to implement the above-mentioned dynamic system. The variational weak form is the bridge that connects the mathematical strong form of variables such as ϕ and σ, and the software implementation of solving them. Therefore, we list the weak forms of the simulated systems in the rest of this section. In the weak form equations, we use $x^{(n)}$ to denote the value of x at the nth simulated time step.

We list the derived weak form equations of electrical potential u, phase field ϕ, and hydrostatic stress σ in the following.

1) Electrical Potential: Since EM analysis is done on a time scale of at least days, we treat the electrical potential distribution u as quasi-static so that it can be described by the strong form Laplace equation

$$\nabla \cdot \left(\frac{1}{\rho(\phi)} \nabla u \right) = 0 \quad \text{in } \Omega_L \tag{25}$$

$$u = g_u \quad \text{on } \partial\Omega_L \cap \Gamma_u \tag{26}$$

$$\vec{n} \cdot \frac{1}{\rho(\phi)} \nabla u = g_j \quad \text{on } \partial\Omega_L \cap \Gamma_j \tag{27}$$

where Ω_L is the domain of the simulated copper, $\partial\Omega_L$ is its boundary, $\rho(\phi)$ is the copper resistivity that is implied by the phase field, Γ_u is the boundaries where Dirichlet (voltage) conditions are applied, Γ_j is the boundaries where Neumann (normal current flux) conditions are applied. Multiplying the shape function φ on both side of (25) and (27), the corresponding electrical potential weak form can be derived by applying divergence theorem

$$\int_{\Omega_L} \nabla u \cdot \nabla \varphi \, dV = \int_{\partial\Omega_L} g_j \varphi \, dS \tag{28}$$

where dV is for volume integration and dS is for the surface integration.

2) Phase Field: To discretize time variable t in (18), we, respectively, substitute $\partial\phi/\partial t$ with $(1/\Delta t)(\phi^{(n)} - \phi^{(n-1)})$, ϕ with $\theta\phi^{(n)} + (1-\theta)\phi^{(n-1)}$ to numerically solve the equation based on the Euler method. The superscript n is for time step index. By applying the divergence theorem and collecting $\phi^{(n)}$ related terms on the left-hand side, we have the

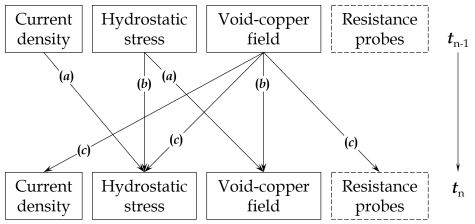

Fig. 3. Block diagram of time-dependent FEM systems coupling. Labels in parenthesis: type of major contribution. (a) Source term. (b) Diffusion term. (c) Material indicator.

time-discretized weak form of (18)

$$\int_{\Omega_L} \phi^{(n)} \varphi \, dV + \int_{\Omega_L} \frac{\delta^2 \theta \Delta t}{2\tau_\phi} \nabla \phi^{(n)} \cdot \nabla \varphi \, dV = \int_{\Omega_L} \phi^{(n-1)} \varphi \, dV - \int_{\Omega_L} \frac{\delta^2 (1-\theta) \Delta t}{2\tau_\phi} \nabla \phi^{(n-1)} \cdot \nabla \varphi \, dV + \int_{\Omega_L} \frac{\Delta t}{\tau_\phi} (\phi^{(n-1)} - (\phi^{(n-1)})^3) \varphi \, dV - \int_{\Omega_L} \Delta t k_R \vec{v} \cdot \nabla \phi^{(n-1)} \varphi \, dV \tag{29}$$

where θ is the Euler method controller ($\theta = 0$: backward Euler; $\theta = 1$: forward Euler; $\theta = (1/2)$: mixed Euler or Crank–Nicolson method). We use Crank–Nicolson method ($\theta = (1/2)$) since it has the stability like backward Euler method and also higher (second order) accuracy. Δt is the time-discretization step which is a knob for controlling the solution accuracy.

3) Hydrostatic Stress: We perform similar time discretization and mathematics techniques on hydrostatic variable σ to get the following weak form of (2) and (22)

$$\int_{\Omega_L} \left(1 + \left(\frac{w_V}{\tau_{\text{void}}} - \frac{|v| k_\tau w_B}{\delta}\right) \theta \Delta t\right) \sigma^{(n)} \varphi \, dV + \int_{\Omega_L} (w_B + w_C) \frac{D_a B \Omega}{k_B T} \theta \Delta t \nabla \sigma^{(n)} \cdot \nabla \varphi \, dV = \int_{\Omega_L} \left(1 - \left(\frac{w_V}{\tau_{\text{void}}} - \frac{|v| k_\tau w_B}{\delta}\right) (1-\theta) \Delta t\right) \sigma^{(n-1)} \varphi \, dV - \int_{\Omega_L} (w_B + w_C) \frac{D_a B \Omega}{k_B T} (1-\theta) \Delta t \nabla \sigma^{(n-1)} \cdot \nabla \varphi \, dV + \int_{\Omega_L} \Delta t w_C \frac{D_a B \Omega}{k_B T} e Z \nabla \sigma^{(n-1)} \cdot \nabla \varphi \, dV + \int_{\partial \Omega_L} \Delta t w_C \frac{D_a B}{k_B T} e Z \rho j_{N_i} \cdot \vec{n} \varphi dS, \tag{30}$$

where j_{N_i} denotes the prescribed normal current densities as described in (2).

With the weak forms (28), (29), and (30), the EM solver is able to calculate the integrals to assemble the FEM matrices and input loads, and solve for space- and time-discretized solutions.

B. Adaptive Local Mesh Refinement

When solving FEM problems, adaptive local mesh refinement is crucial to achieve desired precision in detail-rich parts of a domain without wasting computation resources in portions with relatively smoother solutions. Essentially, adaptive local mesh refinement allows relatively coarse initial mesh and then refines the mesh according to the analysis of the solution of each time step.

On each time step, which is solved using the backward Euler method, each physical system is updated according to the dependencies specified in Fig. 3. We use Rothe's method [19] to discretize the time variable first and then the spatial variables (meshing). Given the nature of the moving copper void boundary (implied by the phase field), it requires varying the location of highly locally refined mesh over time. Therefore, a method of lines [20] which discretize the space variables first and then time variable, not allowing time-dependent local mesh refinement is not suitable for the implementation of the proposed method.

Kelly estimator [21] is used to do posterior error estimation on finite elements. According to the estimated error, adaptive refinement is conducted on the original coarse grid, which is meshed by Gmsh [22]. Since the three systems have solutions in very different scales, the synthesized error can easily be dominated by one system. We use a normalize-then-scale method to mitigate this problem and provide an adjustable knob to fine-tune the adaptive mesh refinement. Respectively, let $\hat{\epsilon}_P$, $\hat{\epsilon}_E$, and $\hat{\epsilon}_S$ denote the estimated error vector of copper void phase field, electrical potential, and hydrostatic stress, which are all normalized to [0, 1], we synthezise the final error vector using a weighted sum

$$\bar{\epsilon} = c_P \hat{\epsilon}_P + c_E \hat{\epsilon}_E + c_S \hat{\epsilon}_S \tag{31}$$

where c_P, c_E, and c_S are the weighting factors for the physics systems.

Fig. 4 shows the outcome of the refinement. Comparing to the previous refinement step ($t = 0$), hydrostatic stress is evenly distributed over the copper so the mesh does not get coarsened, except for the void-copper boundary and a high-current-density corner. When the stress starts to grow, the normalize-then-scale algorithm synthesizes the errors generated by Kelly estimator and effectively indicates the correct position to be refined. The refinement behavior is determined by the solution while time-dependent analysis is being performed. This is helpful as the characteristics of underlying physical systems are not required to be considered when generating the initial mesh. Instead, only very coarse mesh that merely describes the structure is needed. It is beneficial since the interfacing to automatic interconnect structure generation can be dramatically simplified.

C. Software Implementation

The proposed method is implemented using the deal.II FEM library [18]. The algorithm flow of the proposed postvoiding EM FEM solver is shown in Fig. 5. The input mesh is in Gmsh [22] format version 2.2. Only a coarse mesh that is enough to describe the geometry structure is required. The mesh is then refined according to the analysis of the solution. All the parameters, including technology parameters, finite-element configurations, solver setups, and PDE configurations, can be easily adjusted by specifying in the input

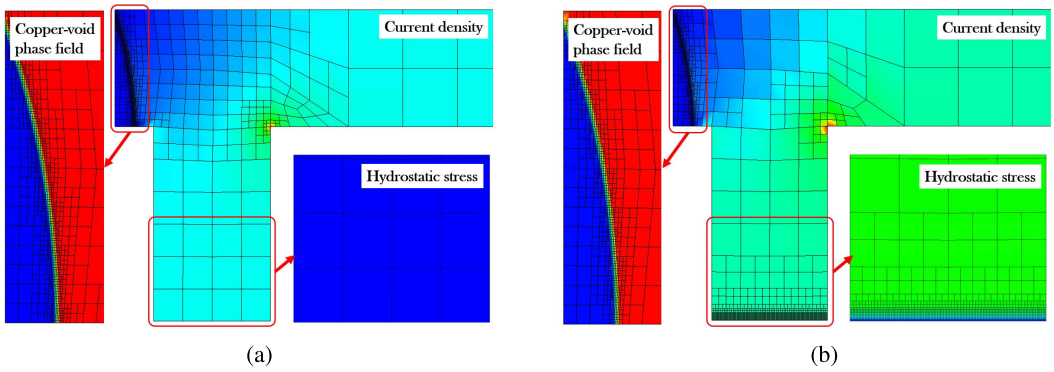

Fig. 4. Adaptive local refinement of hydrostatic stress solution while phase field is fixed. (a) Before refinement. (b) After refinement.

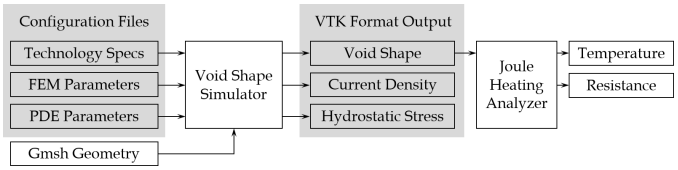

Fig. 5. Algorithm flow of the proposed postvoiding EM FEM simulator.

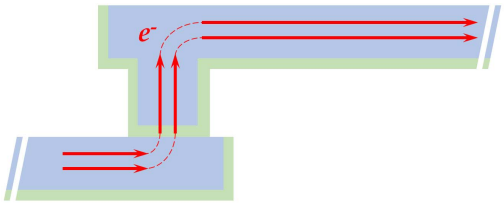

Fig. 6. Illustration of electron flow (marked as e^-) in an upstream configuration.

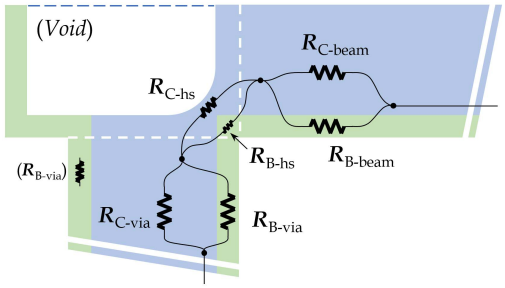

Fig. 7. Discretized approximation of metal connectivity before the temperature jump.

parameter file. The simulation result is in visualization toolkit format [23], which is widely used in scientific computing community for scalable and efficient postprocessing and rendering. The software is modularized and divided into the following physical systems with minimized coupling: electrical potential system, phase field system, hydrostatic stress system, and resistance probes system. The resistance probes system are similar to the electrical potential system but they only apply voltage on certain user-specified boundary pairs in order to measure resistance, without affecting the hydrostatic stress. Resistance probes system is governed by (25), (26), and (28) as well.

IV. Simulation of Joule Heating Effect

Void growth simulation enables observing temperature and resistance jump due to Joule heating effect. Under an upstream configuration, where electron flows from via to upper level of copper interconnect as illustrated in Fig. 6, a temperature and resistance jump is observed in [24]. When a growing void, expanding from the reservoir side toward the anode direction, covers all the via copper, the current originally conducting by copper will be shunted to the surrounding barrier metal. As shown in Fig. 7, the current flows through a narrow portion of barrier metal in such case, where the Joule heating is highly concentrated and heat dissipation is limited. We refer this portion of the barrier, and the copper (if any) close by, as *the hotspot*. A hotspot is suddenly heated up at the time the via copper is cutoff from the main interconnects by the growing void. Consequently, the temperature will noticeably increase near the hotspot. It should be noted that under a prescribed current density, hotspot temperature, and resistance will converge at a higher level due to a weak positive feedback in between. To be specific, higher temperature leads to higher hotspot resistance (given their positive resistivity temperature coefficient), followed by higher Joule heating power, which feeds back to higher temperature. The convergence of the hotspot temperature and resistance is guaranteed since: 1) a realistic metal or alloy has low resistivity temperature coefficient (usually less than 0.01) and 2) temperature itself is in a negative feedback loop because heat dissipation rate is proportional to media temperature difference, according to Fourier's law of thermal conduction.

Figs. 7 and 8 illustrate how the electrical connectivity is modeled. The total resistance is calculated using

$$R = (R_{\text{C-via}} \| R_{\text{B-via}}) + (R_{\text{C-hs}} \| (R_{\text{B-hs}} + R_{\text{B-neck}})) + (R_{\text{C-beam}} \| R_{\text{B-beam}}) \quad (32)$$

where "$\|$" is the impedance parallel operator: $z_1 \| z_2 = (z_1\ z_2 / z_1 + z_2)$, subscript prefix "C-" and "B-," respectively, denotes *copper* and *barrier*, subscript postfix "-hs" stands for *hotspot*.

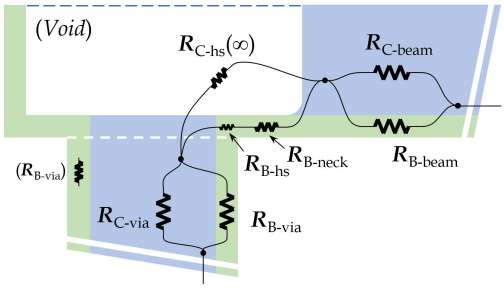

Fig. 8. Discretized approximation of metal connectivity after the temperature jump.

On the hotspot, the temperature is modeled by balancing the heat dissipation and generation

$$\frac{\lambda A(T-T_0)}{\delta} = I^2[R_{\text{B-hs}}(1+\alpha_B(T-T_{\text{ref}})) \| R_{\text{C-hs}}(1+\alpha_C(T-T_{\text{ref}}))] \quad (33)$$

where λ is the heat conduction coefficient; T is the temperature to solve; T_0 is the temperature of the surrounding metal; T_{ref} is the reference temperature for barrier resistivity calculation; α_B and α_C are, respectively, the resistivity of the barrier material and copper; A and δ are the effective heat dissipation area and thickness, respectively; and I is the prescribed electrical current. We assume that the heating hotspot is small when compared to the interconnect scale such that the temperature surrounding metal does not change much because of the hotspot. $R_{\text{B-hs}}$ can be calculated as a constant since the barrier does not have structure change while the void is evolving. Copper resistance at the hotspot $R_{\text{C-hs}}$ can be measured by applying probes during simulation. Note that in Figs. 7 and 8, due to its 2-D nature, it cannot fully demonstrate the barrier connectivity in 3-D cases. The green-shaded barrier material on the left side and right side are actually mechanically and electrically connected in 3-D cases, as they are surrounding the copper interconnect except near the copper capping layer boundary. Here, capping layer refers to the isolation layer in dual-damascene process [25]. $R_{\text{B-hs}}$, $R_{\text{B-via}}$, and $R_{\text{B-neck}}$ are, therefore, not as separable in 3-D as in the illustrated 2-D case.

By collecting all the above-mentioned values, the temperature change caused by Joule heating can be calculated. According to (32) and (33), resistance change, and temperature change can be divided into three phases.

In the first phase, when the hydrostatic stress is not built up to the critical level to drive the void to grow, or the growing void is still mostly contained in the reservoir, thus the resistance of copper at the hotspot remains approximately unchanged. In this phase, the total resistance temperature does not change noticeably over time, since the structure of conducting material is not changed. Consequently, the heating characteristic and temperature stay approximately unchanged.

In the second phase, the void size is large enough to partially cover the via cross section area. As depicted in Fig. 7, a large portion of the copper that conducts the current between the via and the rest of the interconnect (marked as *beam*) has been depleted. This will cause the effective resistance $R_{\text{C-hs}}$ to noticeably increase, compared to the first phase. It keeps increasing until there is no copper connecting the via and the *beam*, where effectively, $R_{\text{C-hs}} = +\infty$. During the end of this phase, $R_{\text{C-hs}}$ accelerates approaching infinity, as the effective hotspot copper conductivity (reciprocal to resistivity) decreases to zero, with the void growing at a steady speed. In this phase, $R_{\text{C-hs}}$ and $R_{\text{B-hs}}$ dominates the whole resistance growth.

In the third phase, it is merely the barrier material that conducts current between the via and the rest of the copper. We use $R_{\text{B-neck}}$ to denote this part of the barrier, next to which the copper is already depleted in the previous phases. As the void continues to grow, $R_{\text{B-neck}}$ increases due to Ohm's law. Comparing to the second phase, $R_{\text{B-neck}}$ dominates the whole resistance growth in this phase and increases linearly as the void growing at a steady speed.

V. Numerical Results and Discussion

We conduct three sets of experiments to verify the effectiveness of the proposed method. We first conduct experiments in 1-D, 2-D, and 3-D to verify the capability of simulating at different levels of dimensional abstractions. In each experiment, we visualize the simulation result with different aspects emphasized. We thoroughly discuss the observation and how they prove the proposed simulation method to be consistent with the experimental observations and accepted modeling works. To further support this, in the second experiment, we measure the failure time of a group of simulations applied with different current densities to compare the mean TTF (MTTF) measured in two experiments and a model proposed in [7]. In the third experiment, from a simulated void growth in an upstream-configured copper wire, we observe the temperature and resistance jump due to Joule heating effect, which can be verified by a realistic EM reliability experiment in [24].

A. Simulations of Different Levels of Dimensional Abstractions

In cases that void shapes are allowed to be abstracted into lower dimensional representations, 1-D and 2-D simulations have advantages of their relatively lighter computational demand. Therefore, it is important to verify the sanity of void size, stress evolution, as well as the reasonableness of adaptive local mesh refinement. In the simulated copper domain, since the void size is regulated by the integral of the hydrostatic stress, it allows us to simulate the interconnects with different numbers of dimensions abstracted out without losing the consistency between the void size and the distribution of hydrostatic stress. On the other hand, inward and outward electrical current on the interconnect boundary, respectively, provides the hydrostatic stress sink and source, which do not lose their generality because of dimensional abstraction (from 3-D toward 2-D, or 1-D).

Fig. 9 shows a 3-D growing void simulation using the proposed method. It is shown that once a void has nucleated, which is typically at or near a terminal node, the stress around the void will immediately become zero (where element entities are removed to better demonstrate the void shape). However, the stress around the void will be close to the same stress level

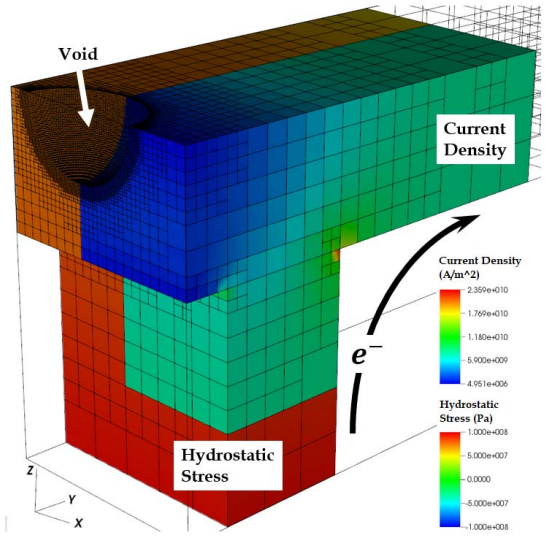

Fig. 9. Three-dimensional void growth simulation of a 20-μm upstream-configured copper interconnect. The interconnect is cut into two portions for visualization: front showing current density and back showing hydrostatic stress.

as immediately prior to the nucleation [8], [13]. A very large stress gradient will be formed around the void at nucleation time, which can be described by [13]. As a result, at steady state, hydrostatic stress around the cathode and the void will be at near-zero level because of the stress relaxation introduced by the advancing copper void boundary. Mesh is locally refined near the void boundary to deliver better accuracy of void shape calculation.

As shown in Fig. 9, local mesh refinement is reasonably applied in different locations in the domain so that all three physical systems can have smooth solutions. On void-copper boundary, where phase field has a large gradient, the mesh gets refined to acquire better solution accuracy. On the corner, where the current density is high, mesh gets refined but still remains relatively coarse compared to the copper void boundary, as configured by parameter c_E. We use such a configuration since the current density accuracy is not as prioritized as the phase field and hydrostatic stress. At the cathode end, where the mesh was previously refined (as demonstrated in Fig. 4 at $t = 0$), is now dramatically coarsened since the stress has been evolved to be smooth enough at the point. On the rest of the area, where solutions of all three systems are relatively smooth in space, the mesh remains coarse. This leads to smaller sparse system matrix requiring less computational resources.

Figs. 10 and 11 illustrate the snapshots taken on void shape, hydrostatic stress, and a current density of two 2-D simulations on a 20-μm upstream-configured copper interconnect. Because of the nature of the phase-field representation of the void-copper material, as the void boundary moves, it can move across vertices in the simulated geometry without altering the finite-element system matrix structure. As shown in the figure, hydrostatic stress grows at the cathode end until it reaches the critical stress and then the void starts to grow. After the void started to grow, the moving void-copper boundary introduces a hydrostatic stress sink due to the material migration, as mentioned in (20). This is the reason that the cathode hydrostatic stress is decreasing later. Therefore, the cathode hydrostatic stress is observed to be first increasing then decreasing, which agrees with the behavior described in the nucleation phase and growth phase.

TABLE I
PARAMETERS USED IN VOID GROWTH SIMULATION

Symbol	Value	Description
D_a	$5.2 \times 10^{-6}\text{m}^2/\text{s}$	Diffusion coefficient
Z	-5	Effective charge number
δ	2nm	Boundary thickness
E_a	0.9eV	EM activation energy
B	110GPa	Effective bulk modulus
T	350K	Operation temperature
θ	0.5	Backward-Euler previous step weight
τ_{void}	1s	Stress vanishing characteristic time
τ_ϕ	1000s	Phase field converging characteristic time
k_τ	1	Stress vanishing speed-up factor
k_s	50	Material indicator sharpness
ϕ_{th}	0.95	Material indicator threshold
c_P	1	Kelly error weight of phase field
c_E	50	Kelly error weight of voltage
c_S	40	Kelly error weight of stress

1-D simulations are conducted on a 30-μm copper interconnect. As shown in Fig. 12 (magnified details in Fig. 13), it is easier to visualize the stress evolution over the simulated interconnect over time. Under a steady current applied toward the $-x$-direction, the stress converges at a steady state where the linear transition starts from zero near the cathode/void boundary to its minimum value (maximum compressive stress). The increase-then-decrease in hydrostatic stress observed near the cathode agrees with the 2-D simulation as well. In the zoomed-in view in Fig. 13, the leftmost section with zero stress indicates the void. It is clear to see that the copper void boundary, which is indicated by the following increasing edges, advances toward the $+x$-direction. It is important to mention that the void size does not increase until the cathode hydrostatic stress builds to a critical level at the cathode, which is a strong evidence that the void nucleation phase and growth phase are integrated as a whole in the proposed FEM simulation method.

B. Calculation of Time to Failure

In this section, we present TTF simulation results and comparison and existing modeling methods and two real chip experiments. In the simulation, we use the parameters specified in Table I.

With different current densities applied, void saturates at different sizes, as shown in Fig. 14. Compared to experimental results, the simulated hydrostatic stress is expected to grow fast at an early stage because of large current flux and slowly drops because of the advancement of copper void boundary. We can successfully observe that the hydrostatic stress accumulated at the void end is absorbed by the advancing copper void boundary and stops on a relatively low level when the void is saturated. Under the extreme condition of current density applied on a copper line having enough length, we observe EM open-circuit failure before the void saturates.

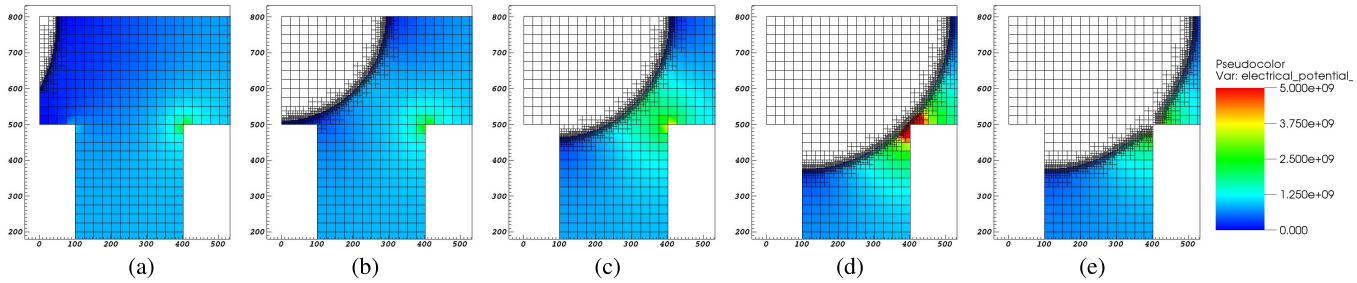

Fig. 10. Current density and void growth simulation of a 20-μm upstream-configured copper interconnect (zoomed-in views of the cathode end, axis unit: nanometer). (a) $t = 0$ h. (b) $t = 1990$ h. (c) $t = 3200$ h. (d) $t = 4130$ h. (e) $t = 4160$ h.

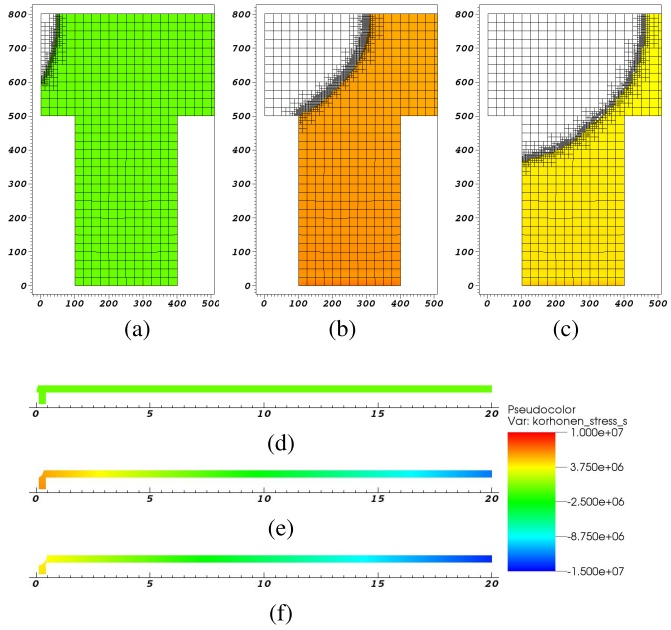

Fig. 11. Hydrostatic stress and void growth simulation of a 20-μm upstream-configured copper interconnect. (a)–(c) Zoomed-in views, axis unit: nanometers. (d)–(f) Overviews, axis unit: micrometers.

The widely used statistical MTTF estimation for EM wear out is given by Black's equation [4]

$$\text{MTTF} \approx A j^{-n} \exp\left(\frac{E_a}{k_B T}\right) \tag{34}$$

which empirically shows the relationship between current density and MTTF. Under certain operating temperature, the simulated MTTF should satisfy (34). To check the consistency with the MTTF experimental relationship (MTTF) $\propto j^{-n}$, we fit the exponent n using least squares method.

Fig. 15 shows the fit exponent n under different operating temperature compared with two experimental results measured in [26] and [27]. We also compare our result against a recently published work [8], which focuses on the stress development in the copper wire without considering their impacts on the void volume. As we can see, the proposed FEM analysis method fits better against the two measured results than the recently published work, especially at high temperature [8].

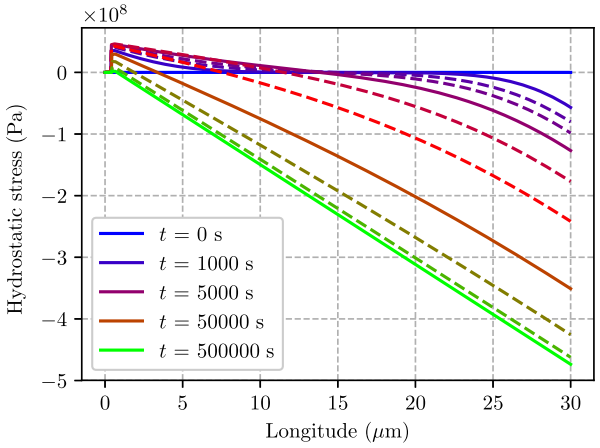

Fig. 12. Hydrostatic stress evolution on a 30-μm copper interconnect.

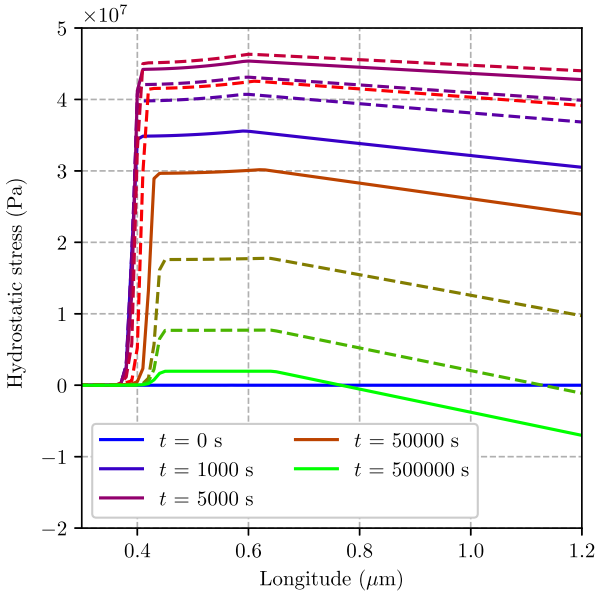

Fig. 13. Hydrostatic stress evolution on a 30-μm copper interconnect magnified at near cathode/void position.

C. Wire Resistance Changes and Joule Heating

To validate the proposed FEM analysis method, in this section, we show that the proposed EM analysis can predict the wire resistance change patterns over time and Joule heating effects, which were observed experimentally [24], [28].

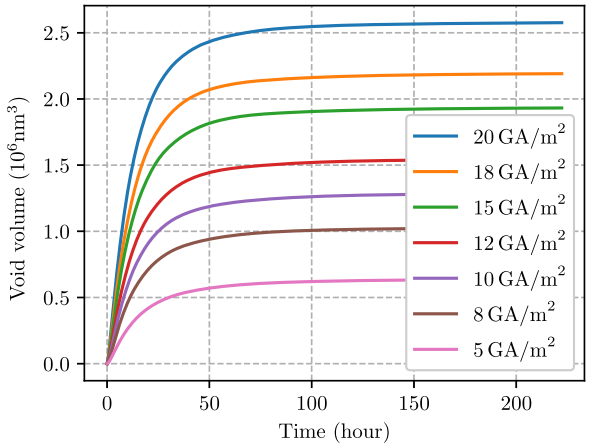

Fig. 14. Void size versus time with different current densities (GA: 10^9A) applied.

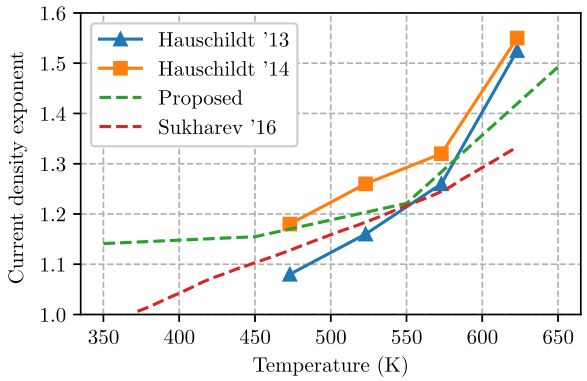

Fig. 15. Extracted current density exponent n compared to two experiments [26], [27], and a recent postvoiding EM analysis work [8].

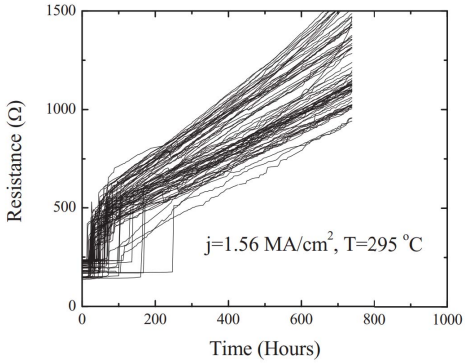

Fig. 16. Resistance change of copper interconnects over time measured in experiment [24].

Fig. 16 shows the measured time-dependent resistance change of different interconnect wires during test stressing. As we can see, wire resistance initially does not change until an abrupt resistance jump. This happens when all the current starts to flow over the barrier layers as void reaches a critical size, by the time the growing void covers the via and separates the via copper from the main conducting part. Also, the abrupt resistance change is believed to be due to Joule heating in the barrier layers. Since barrier material has higher resistance and very limited cross section area conducting current, an increment of total effective resistance and temperature should be observed. We collect simulation data from an upstream-configured 20-μm copper interconnect,

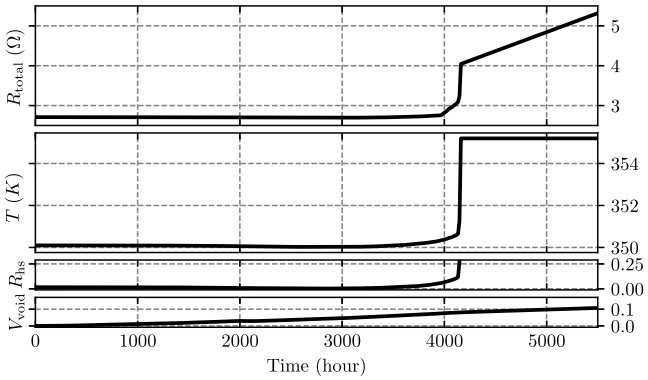

Fig. 17. Simulation of Joule heating effect. R_{total}: total wire resistance. T: temperature at the hotspot. R_{hs}, in ohms: copper resistance at the hotspot. V_{void}, in cubic micrometer: simulated void size.

stressed under a constant current density of 4×10^{10} A/m^2 to expect early failure. As shown in Fig. 17, the temperature and resistance change can be divided into four stages.

In the first stage (t/hour < 3000), only the increasing void size can be observed while total effective resistance change is negligible. This is because the growing void is still majorly contained by the designated reservoir and does not cut into the main current conducting channel. In this stage, nontrivial temperature increase is not observed either.

In the second stage ($3000 < t$/hour < 4150), void starts to cut into and occupy the main channel. As a consequence, increasing of both hotspot resistance and effective total interconnect resistance is observed. Before the hotspot resistance reaches infinity (copper open circuit), barrier material shunts an increasing portion of total current in parallel with the copper at the hotspot.

The third stage (t/hour ≈ 4150), is the instant, or the relatively short time span during the total simulated EM failure process, the copper interconnect is separated by the void at the hotspot. Consequently, the hotspot barrier carries all the prescribed current and generates significantly more Joule heat compared to the case without the void. Since the hotspot is a small volume, having high resistance and limited dissipation area, significant resistance and temperature jump are observed, which matches the analysis in Section IV.

In the fourth stage (t/hour > 4150), void size keeps growing into the metal layer copper branch. As copper is voided, the current is shunted onto the adjacent barrier material, which leads to the increase of the total effective resistance. Despite this, at this phase, we do not observe the noticeable temperature change. This is because the resistance added later corresponds to relatively large portion of barrier material, which has enough dissipation area to dissipate heat into the surrounding metal.

The above-mentioned observation matches the analysis in Section IV and the experiment data collected in [24]. This validates that the simulation method is consistent with the practical EM failure process.

VI. Conclusion

In this paper, we have proposed a novel FEM-based stress simulation method for fast EM failure analysis. To explicitly model the void boundary movement, we introduced a

phase-field variable governed by the PDEs, which results in two coupled dynamic systems to describe the whole postvoiding stress evolution process. To incorporate the inherent physical interaction between the void volume and stress distribution in a confined interconnect wire due to atomic conservation, a regulation factor for void growth velocity is introduced such that the void boundary movement speed is controlled to ensure the atomic conservation. Numerical results show that the calculated stress distributions and extracted current exponent values fit better with the measured results than a recent proposed postvoiding analysis method. Furthermore, the proposed EM analysis method can simulate Joule heating effects on wire resistance and temperature, and thus, captures the unique transient wire resistance change pattern that is observed by the published experimental data.

REFERENCES

[1] (2015). *International Technology Roadmap for Semiconductors (ITRS)*. [Online]. Available: http://public.itrs.net

[2] B. Bailey, "Thermally challenged," *Semicond. Eng.*, pp. 1–8, Dec. 2013.

[3] S. X.-D. Tan, H. Amrouch, T. Kim, Z. Sun, C. Cook, and J. Henkel, "Recent advances in EM and BTI induced reliability modeling, analysis and optimization," *Integr., VLSI J.*, vol. 60, pp. 132–152, Jan. 2018.

[4] J. R. Black, "Electromigration—A brief survey and some recent results," *IEEE Trans. Electron Devices*, vol. 16, no. 4, pp. 338–347, Apr. 1969.

[5] I. A. Blech, "Electromigration in thin aluminum films on titanium nitride," *J. Appl. Phys.*, vol. 47, no. 4, pp. 1203–1208, Apr. 1976.

[6] X. Huang, A. Kteyan, X. Tan, and V. Sukharev, "Physics-based electromigration models and full-chip assessment for power grid networks," *IEEE Trans. Comput.-Aided Design Integr. Circuits Syst.*, vol. 35, no. 11, pp. 1848–1861, Feb. 2016.

[7] V. Sukharev, A. Kteyan, and E. Zschech, "Physics-based models for EM and SM simulation in three-dimensional IC structures," *IEEE Trans. Device Mater. Rel.*, vol. 12, no. 2, pp. 272–284, Jun. 2012.

[8] V. Sukharev, A. Kteyan, and X. Huang, "Postvoiding stress evolution in confined metal lines," *IEEE Trans. Device Mater. Rel.*, vol. 16, no. 1, pp. 50–60, Mar. 2016.

[9] H.-B. Chen, S. X.-D. Tan, X. Huang, T. Kim, and V. Sukharev, "Analytical modeling and characterization of electromigration effects for multibranch interconnect trees," *IEEE Trans. Comput.-Aided Design Integr. Circuits Syst.*, vol. 35, no. 11, pp. 1811–1824, Nov. 2016.

[10] C. Chen, S. X.-D. Tan, J. Peng, T. Kim, and J. Chen, "Analytical modeling of electromigration failure for VLSI interconnect tree considering temperature and segment length effects," *IEEE Trans. Device Mater. Rel.*, vol. 17, no. 4, pp. 653–666, Dec. 2017.

[11] Z. Sun, E. Demircan, M. D. Shroff, C. Cook, and S. X.-D. Tan, "Fast electromigration immortality analysis for multi-segment copper interconnect wires," *IEEE Trans. Comput.-Aided Design Integr. Circuits Syst.*, to be published.

[12] C. Cook, Z. Sun, E. Demircan, M. D. Shroff, and S. X.-D. Tan, "Fast electromigration stress evolution analysis for interconnect trees using Krylov subspace method," *IEEE Trans. Very Large Scale Integr. (VLSI) Syst.*, vol. 26, no. 5, pp. 969–980, May 2018.

[13] M. A. Korhonen, P. Bo-Rgesen, K. N. Tu, and C.-Y. Li, "Stress evolution due to electromigration in confined metal lines," *J. Appl. Phys.*, vol. 73, no. 8, pp. 3790–3799, 1993.

[14] E. T. Ogawa, K.-D. Lee, V. A. Blaschke, and P. S. Ho, "Electromigration reliability issues in dual-damascene Cu interconnections," *IEEE Trans. Rel.*, vol. 51, no. 4, pp. 403–419, Dec. 2002.

[15] C.-K. Hu, M. Small, and P. Ho, "Electromigration in Al(Cu) two-level structures: Effect of Cu and kinetics of damage formation," *J. Appl. Phys.*, vol. 74, no. 2, pp. 969–978, 1993.

[16] M. A. Korhonen, P. Bo/rgesen, D. D. Brown, and C.-Y. Li, "Microstructure based statistical model of electromigration damage in confined line metallizations in the presence of thermally induced stresses," *J. Appl. Phys.*, vol. 74, no. 8, p. 4995, 1993.

[17] D. N. Bhate, A. F. Bower, and A. Kumar, "A phase field model for failure in interconnect lines due to coupled diffusion mechanisms," *J. Mech. Phys. Solids*, vol. 50, no. 10, pp. 2057–2083, 2002.

[18] D. Arndt *et al.*, "The deal. II library, version 8.5," *J. Numer. Math.*, vol. 25, no. 3, pp. 137–145, 2017.

[19] J. Kačur, "Method of rothe in evolution equations," in *Equadiff 6* (Lecture Notes in Mathematics). Springer, 1986, pp. 23–34.

[20] R. Pregla and W. Pascher, "The method of lines," *Numer. Techn. Microw. Millim. Wave Passive Struct.*, vol. 1, pp. 381–446, 1989.

[21] D. W. Kelly, J. P. D. S. R. Gago, O. C. Zienkiewicz, and I. Babuska, "*A posteriori* error analysis and adaptive processes in the finite element method: Part I—Error analysis," *Int. J. Numer. Methods Eng.*, vol. 19, no. 11, pp. 1593–1619, 1983.

[22] C. Geuzaine and J.-F. Remacle, "Gmsh: A 3-D finite element mesh generator with built-in pre- and post-processing facilities," *Int. J. Numer. Methods Eng.*, vol. 79, no. 11, pp. 1309–1331, 2009.

[23] R. Wang, T. Benner, A. G. Sorensen, and V. J. Wedeen, "Diffusion toolkit: A software package for diffusion imaging data processing and tractography," in *Proc. Int. Soc. Magn. Reson. Med.*, Berlin, Germany, vol. 15, 2007, p. 3720.

[24] R. G. Filippi, P.-C. Wang, A. Brendler, K. Chanda, and J. R. Lloyd, "Implications of a threshold failure time and void nucleation on electromigration of copper interconnects," *J. Appl. Phys.*, vol. 107, no. 10, p. 103709, 2010.

[25] A. Grill, J. P. Hummel, C. V. Jahnes, V. V. Patel, and K. L. Saenger, "Dual damascene processing for semiconductor chip interconnects," U.S. Patent 6 140 226, Oct. 31, 2000.

[26] M. Hauschildt *et al.*, "Electromigration void nucleation and growth analysis using large-scale early failure statistics," in *Proc. AIP Conf.*, vol. 1601, no. 1, 2014, pp. 89–98.

[27] M. Hauschildt *et al.*, "Electromigration early failure void nucleation and growth phenomena in Cu and Cu(Mn) interconnects," in *Proc. IEEE Int. Rel. Phys. Symp. (IRPS)*, Apr. 2013, pp. 2C.1.1–2C.1.6.

[28] L. Zhang, "Effects of scaling and grain structure on electromigration reliability of cu interconnects," Ph.D. dissertation, Dept. Elect. Comput. Eng., Univ. Texas Austin, Austin, TX, USA, 2010.

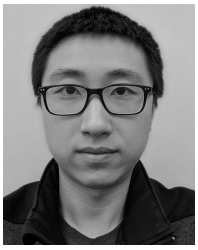

Hengyang Zhao received the B.S. degree in computer science and the M.S. degree in metering and instrumentation engineering from Shanghai Jiao Tong University, Shanghai, China, in 2011 and 2014, respectively. He is currently working toward the Ph.D. degree in electrical engineering at the University of California at Riverside, Riverside, CA, USA.

His current research interests include VLSI reliability modeling, smart building energy optimization, finite-element method-based simulation, and machine learning applications.

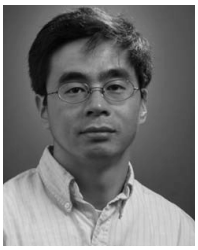

Sheldon X.-D. Tan (S'96–M'99–SM'06) received the B.S. and M.S. degrees in electrical engineering from Fudan University, Shanghai, China, in 1992 and 1995, respectively, and the Ph.D. degree in electrical and computer engineering from the University of Iowa, Iowa City, IA, USA, in 1999.

He was a Visiting Professor and a JSPS Fellow with Kyoto University, Kyoto, Japan, in 2017. He is currently a Professor at the Department of Electrical Engineering, University of California at Riverside, Riverside, CA, USA, where he is a Cooperative Faculty Member at the Department of Computer Science and Engineering. He is also the Associate Director of Computer Engineering Program at the University of California at Riverside. His current research interests include VLSI reliability modeling, optimization and management at circuit and system levels, thermal modeling, optimization and dynamic thermal management for multicore processors, statistical modeling, simulation and optimization of mixed-signal/RF/analog circuits, and parallel circuit simulation techniques based on GPU and multicore systems.

Dr. Tan was a recipient of the Outstanding Oversea Investigator Award from the National Natural Science Foundation of China in 2008, the NSF CAREER Award in 2004, the Best Paper Award from 2007 IEEE International Conference on Computer Design, the Best Paper Award from 1999 IEEE/ACM Design Automation Conference, the three Best Paper Award Nominations from IEEE/ACM Design Automation Conferences in 2005, 2009, and 2014, and one Best Paper Award Nomination from ASP-DAC in 2015. He is currently serving as the Editor-In-Chief for *Integration, The VLSI Journal*. He is also serving as an Associate Editor for three journals, namely, the IEEE TRANSACTIONS ON VLSI SYSTEMS, *ACM Transactions on Design Automation of Electronic Systems*, and *Microelectronics Reliability*.